

Synthesis of Lattice-Contracted Cobalt Disulfide as an Outstanding Oxygen Reduction Reaction Catalyst via Self-assembly Arrangement

Hao Zhang,^[a] Zhiqiang Wang,^[b] Chenglong Ma,^[a] Zhenhua Zhou,^[a] Limei Cao,^[a] Xueqing Gong,^[b] Chunxiao Dong,^[c] and Ji Yang^{*[a]}

Identifying high-performance non-precious metal-based catalysts at the cathode is a major challenge for future practical applications. Herein, a soft-template route through a self-assembly arrangement of sulfur sources was successfully developed, facilitating the anion exchange. In addition, compared with pristine cobalt disulfide synthesized without templates, the cobalt disulfide prepared using the new method presented a lattice shrinking phenomenon due to the hindrance of cobalt hydroxide crystal cell. Based on X-ray absorption spectroscopy (XAS) and density functional theory (DFT) calculation, increased occupancy of e_g orbitals was verified for the

cobalt disulfide after shrinkage, which was the main factor for enhancing the intrinsic activity of the catalyst. Besides the microscopic morphologic structure, elementary composition, and the valence state of the elements, the possible growth process of the cobalt disulfide was also discussed in detail. As catalyst for the oxygen reduction reaction, CoS_2 showed a similar half-wave potential (0.81 vs. 0.84 V for Pt/C) and higher diffusion-limiting current density (reaching 5.33 vs. 5.19 mA cm^{-2} for Pt/C) than a commercial Pt/C catalyst. Hence, our results provide a rational design direction for this type of catalysts.

Introduction

Fuel cell urgently needs to be developed as a new energy technology to reduce energy consumption and pollution.^[1] However, experience and rare precious Pt-based catalysts as the state-of-the-art oxygen reduction reaction (ORR), toughen the approaching commercialization of fuel cells. Hence transition metal oxides and chalcogenides with inexpensive, abundant, and eco-friendly advantages, have been considered as one of the best alternatives.^[2]

In contrast to metal oxides, metal chalcogenides are a more appealing option because the S3p orbitals are more negative than O2p orbitals when they compose conduction bands of catalysts together with d -orbitals of metal cations, which

indicates that metal chalcogenides can exhibit relatively high conductivity by a shallow band gap.^[1,3] According to recent research,^[4] cobalt sulfides as one kind of promising ORR catalysts have been investigated and applied extensively, such as Co_9S_8 , CoS, Co_3S_4 , CoS_2 , and Co_{1-x}S . As of now, there have many reports about improving the catalytic activity of cobalt sulfides. Typically, Higgins et al.^[5] prepared octahedra CoS_2 in conjunction with different carbon support prepared excellent ORR activity by reinforcing the metal-supports interaction. Incorporating these carbon materials played an essential role in achieving well-defined octahedra CoS_2 that exposing highly active {111} facets for ORR. In addition, Singh et al.^[6] also reported the detailed synthesis conditions of octahedra CoS_2 for regulating facets. Therefore, octahedra CoS_2 tended to have highly reactive surfaces for ORR.

Unlike the shaped-control affecting exposed crystal-planes on the surface of catalysts, the lattice distortion exhibited a direct effect on lattice parameters and thus changed the intrinsic activity of catalysts. In our previous works,^[7] a cation doping strategy to synthesize Cu doping IrO_2 and further affects e_g orbitals occupation of Ir5d electrons. An et al.^[8] reported nanocrystals with subtle lattice distortion in interfaces, and similarly, the distortion had varying degrees of effects on the e_g orbitals occupation of Ni and Cu3d electrons. Therefore, the lattice distortion was a powerful means to regulate the occupation of e_g orbitals that provided a primary descriptor for OER/ORR activity. According to ShaO-Horn and co-workers,^[9] e_g orbitals involved the bonding of oxygenated intermediates on metal ions sites, and was considered as a near-unity occupancy corresponding to highest intrinsic OER/ORR activity, which was usually applied in octahedral crystal field of transition-metal oxides or sulfides. The first shell of the CoS_2 crystal cell was one

[a] H. Zhang, C. Ma, Dr. Z. Zhou, Dr. L. Cao, Prof. J. Yang
State Environmental Protection Key Laboratory of Environmental Risk Assessment and Control on Chemical Processes
School of Resources and Environmental Engineering
East China University of Science and Technology
Shanghai 200237 (P. R. China)
E-mail: yangji@ecust.edu.cn

[b] Dr. Z. Wang, Prof. X. Gong
Key Laboratory for Advanced Materials
Center for Computational Chemistry and Research Institute of Industrial Catalysis
School of Chemistry and Molecular Engineering
East China University of Science and Technology
Shanghai 200237 (P. R. China)

[c] C. Dong
Key Laboratory for Ultrafine Materials of Ministry of Education
Shanghai Engineering Research Center of Hierarchical Nanomaterials
School of Materials Science and Engineering
East China University of Science and Technology
Shanghai 200237 (P. R. China)

Supporting information for this article is available on the WWW under <https://doi.org/10.1002/cssc.202002960>

cobalt ion coordinated with six sulfur anions to form a slightly distorted octahedron. Therefore the CoS_2 was suitable for traditional crystal field theory.^[10]

Herein we developed a simple hydroxide soft template as the precursor for cobalt disulfide synthesis with outstanding oxygen reduction reaction (ORR) activity. The much mesoporous on soft template made for a self-assembled arrangement of sulfur sources, which facilitated the process of anion exchange and further improved the crystallinity of cobalt disulfide. Besides, the cobalt disulfide, formed from the cobalt hydroxide crystal cell, was also hampered by the crystal cell of cobalt hydroxide with smaller lattice parameters than cobalt disulfide. So, it presented a lattice shrinking phenomenon compared to the pristine cobalt disulfide without templates and further affected the occupancy of e_g orbitals of $\text{Co}3d$ electrons. The changed electronic structure was accurately determined by X-ray diffractometry analysis (XRD), Raman spectroscopy, transmission electron microscopy (TEM), X-ray photoelectron spectroscopy (XPS), and X-ray absorption spectroscopy (XAS). In addition, density functional theory (DFT) calculation was also used to simulate cobalt disulfide with a lattice shrinking for investigating the occupancy of e_g orbitals. Therefore, our systematic study about the effect of lattice shrinking on activity can be applied in other such catalysts designing the field for increasing catalyst intrinsic activity.

Results and Discussion

The crystalline structure of as-prepared catalysts was determined by XRD, showed in Figure 1a. It was observed that the O-CoS_2 synthesized with soft-template and pristine CoS_2 could be easily indexed to the CoS_2 phase (PDF 41-1471). However, the prominent diffraction peaks of O-CoS_2 synthesized with soft-template were more explicit and exhibited higher crystal-

linity (45.33%) by calculation, in comparison to pristine CoS_2 (28.55%). The calculation process of crystallinity was achieved by the function of "Profile fitting" in the Jade 9 software. Hence the using soft template was conducive to the formation of CoS_2 NPs. Notably, all diffraction peaks of O-CoS_2 had a different degree of offset towards the high-angle direction, showed in insert a_1 . Moreover, given the phenomenon that the higher the angle of the diffraction peak, the greater the peak shift, a reasonable inference that O-CoS_2 had a lattice shrinking in comparison to pristine CoS_2 .

The Raman spectroscopy was also performed for the crystal structure of samples. As shown in Figure 1b, five phonon modes were clearly assigned in Raman spectra of O-CoS_2 ,^[11] while the pristine CoS_2 with lower crystallinity presented relatively low peak intensity and sharpness. In the crystal structure of CoS_2 , a covalent bond existed between the two nearest sulfur atoms, which can be reflected by the E_g mode, that is, a pure librational vibration for dumbbells. The most salient characteristic peaks located at about 387 cm^{-1} corresponded to the A_g mode, that is, in-phase stretching vibrations of sulfur atoms,^[12] while the peak partially overlapped with A_g peak was $T_g(2)$ mode that was out-of-phase stretching vibrations. The $T_g(1)$ and $T_g(3)$ modes combined different librational and stretching vibration of sulfur atoms. It is observed that an overall hypsochromic shift for O-CoS_2 was compared with pristine CoS_2 , indicating that a shorter bond or higher electron density. Although the shifts of $T_g(1)$ and $T_g(3)$ peaks were not clearly reflected, characteristic peaks of E_g , A_g , and $T_g(3)$ covered almost all librational and stretching vibration of sulfur atoms,^[10] which was clearly illustrated in the insert. Therefore, the results of Raman were consistent with that of XRD.

Further information gained from Fourier-transformed (FT) k^2 -normalized extended X-ray absorption fine structure (Figure 1c), O-CoS_2 had a lower value of R and presented an overall negative offset of shells, versus pristine CoS_2 . The main scattering paths composed of three Co-S shells and a Co-Co shell were explicitly illustrated in the insert. As shown in Figure 1c1, all shells presented different shrinking percentages because the outer shells would be affected by the inner one, except for the first Co-S_1 shell. For investigating the influence of lattice shrinking on coordination number, the peaks of the Co-S_1 shell corresponding to the scattering paths of cobalt cation to six nearest sulfur anions were fitted by IFEFFIT (Interactive XAFS analysis and FEFF fitting, FEFF is effective cured wave scattering amplitude) calculation, displayed in Figure S1 in the Supporting Information. The results showed that O-CoS_2 had a higher value (4.176) of N (coordination number) multiplied by S_0^2 (amplitude attenuation factor) than that of pristine CoS_2 (4.140). Hence, using a soft template improved crystallinity and resulted cobalt disulfides with shorter Co-S bonds and higher coordination numbers.

The morphologies of pristine CoS_2 and O-CoS_2 were observed by field-emission scanning electron microscopy (FESEM) in Figure 2a and 2b. The nanoparticles of O-CoS_2 consisted of large-grain with a well-defined structure of polyhedron and granules with irregular structure. And pristine CoS_2 with uniform sizes showed irregular ellipsoid structure,

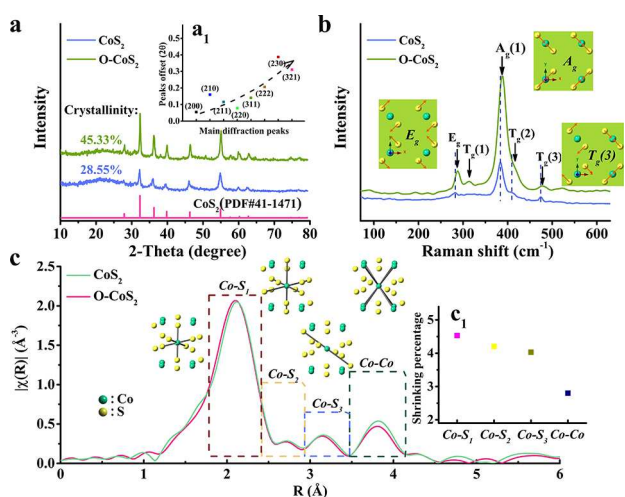


Figure 1. (a) XRD patterns of CoS_2 and O-CoS_2 , inset (a_1) is the peaks offset of sample O-CoS_2 to CoS_2 . (b) Raman spectra of prepared samples and sectional vibration modes. (c) k^2 -normalized CO-K edge EXAFS for prepared samples and inset (c_1) is the shrinking percentage of different shells.

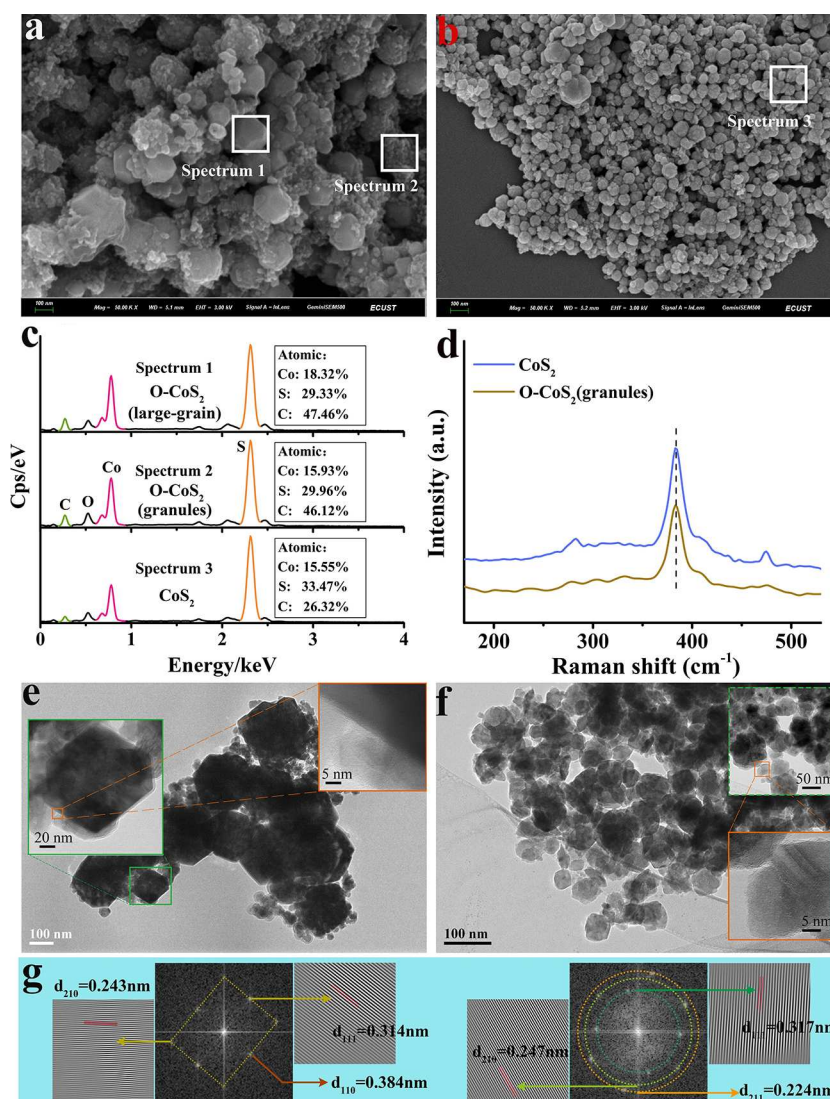


Figure 2. FESEM images of O-CoS₂ (a) and pristine CoS₂ (b). Regional EDS (c) of O-CoS₂ and pristine CoS₂. Raman spectra (d) of CoS₂ and O-CoS₂ (granules). TEM and HRTEM images of O-CoS₂ (e) and pristine CoS₂ (f). Fourier transform graphs (g) of O-CoS₂ and pristine CoS₂.

which was consistent with the previous reports.^[13] N₂ adsorption-desorption isotherms (Figure S2) of pristine CoS₂ and O-CoS₂ clearly identified the pristine CoS₂ (27.04 m²g⁻¹) with the smaller nanoparticles had a higher specific surface area than O-CoS₂ (16.05 m²g⁻¹). To identify the differences of each particle, the regional energy dispersive spectroscopy (EDS) was performed in representative particles, shown in Figure 2c. The large-grain (spectrum 1) displayed a higher ratio of Co: S in comparison to granules (spectrum 2) and pristine CoS₂ (spectrum 3). Increased magnetic Co²⁺ and decreased anaerobic S helped the adsorption of paramagnetic O₂ and the generation of a sulfur vacancy on the surface of CoS₂.^[14] Remarkably, the granules of O-CoS₂ and pristine CoS₂ had a quite close Co: S ratio that was about 1:2 and electronic structure proved by Raman results (Figure 2d). By contrast with highly crystallized O-CoS₂ (large-grain) that was discussed in detail above, the characteristic peak of O-CoS₂ (granules) presented a consistent

peak position (384 cm⁻¹) with pristine CoS₂, indicating the granules of O-CoS₂ had no shrinkage of crystal cell. Therefore, it can be considered that the changes in the electronic structure and electrochemical performances were mainly due to the large-grain of O-CoS₂. Moreover, the regional energy dispersive spectroscopy (Figure 2c), also demonstrated that the NPs of O-CoS₂ had a higher amount of carbon than pristine CoS₂, which can be ascribed to the porous structure of Co-precursor that would be discussed in the following sections.

The difference in morphologies of as-prepared catalysts is further amplified in TEM images. As shown in Figures 2e and f, a clear hexagon is observed on this polyhedron of O-CoS₂ in comparison to irregular pristine CoS₂ NPs. Meanwhile, the phenomenon of lattice shrinking was further bolstered by the lattice spacing derived from the insert of Figure 2e and f. After the Fourier transforms, O-CoS₂ demonstrated a smaller lattice spacing than pristine CoS₂ at the same crystal planes of {210}

and {111}, provided in Figure 2g; that {111} facet is a highly active facet for ORR of CoS_2 has been widely reported.^[5,6] So, the change of lattice spacing in {111} facet inevitably affected the ORR activity. Although well-defined O– CoS_2 was not a regular octahedron, simultaneous exposure of the {111} and {110} facets was an essential characteristic of octahedron- CoS_2 . What is more, the electron diffraction pattern (Figure S3) further demonstrates the difference in crystallinity of pristine CoS_2 and O– CoS_2 . The large-grain of O– CoS_2 (Figure S3c) had significant single crystal diffraction (Figure S3d), and the apparent amorphous halo can be observed in electron diffraction of pristine CoS_2 (Figure S3f) and the granules of O– CoS_2 (Figure S3b).

Proposed growth process

Based on experimental evidence, the possible formation process of O– CoS_2 was illustrated in Figure 3a. Step I was the dissolution of KCl crystal by water, resulting in much mesopore formation on the CO-precursor surface. This phenomenon was consistent with previous reports,^[15] and further demonstrated by Brunner-Emmet-Teller (BET) results, shown in Figure S2 (c and d). Besides, the TEM image of Co–Co precursor (Figure S4)

also observed a clear chiaro-scuro gap and lamellar morphology. These mesoporous played a vital role in the self-assembled arrangement of thiourea (step II) by adsorption, which created a rich sulfur-source environment in favor of anion exchange of S_2^{2-} and OH^- . Also, the microtopography change resulted from the dissolution of potassium chloride crystal might be the cause for the formation of large-grain and granules of O– CoS_2 , which also caused the difference in crystallinity that was higher on the areas with more aggregation of thiourea. The XRD pattern of the sample that skipped the step of I during the synthesis process was also provided in Figure S5 and displayed a wide peak structure without any characteristic peaks. Moreover, the lattice shrinking occurred in step III. It was observed that the crystal lattices of Co(OH)_2 exhibited smaller lattice sizes of $a = b = 3.179 \text{ \AA}$ than that of CoS_2 was $a = b = 3.909 \text{ \AA}$. During the conversion from tetragonal to cubic crystal systems, the growth of CoS_2 was suppressed by Co(OH)_2 crystal cells. Therefore, the O– CoS_2 with soft-template presented a lattice shrinking in comparison to pristine CoS_2 without soft-template.

As provided in Figure 3b, the Co2p spectra were divided into two main peaks and four minor peaks. The main peaks corresponding to $\text{Co}2\text{p}_{3/2}$ and $\text{Co}2\text{p}_{1/2}$, respectively, established an energy separation of 15.1 eV,^[16] which indicated that the oxidation state of cobalt was Co^{2+} . The two minor peaks identified at lower binding energies could be attributed to satellite shake-up peaks,^[17] and that at higher binding energies could be the presence of Co–NH bonds formed by the decomposition of thiourea.^[6,18] The deconvoluted S2p spectra (Figure 3c) show two prominent peaks corresponding to $\text{S}2\text{p}_{3/2}$ and $\text{S}2\text{p}_{1/2}$, respectively, and three minor peaks.^[19] Considering the binding energies of Co2p spectra, the O– CoS_2 exhibited more severe ion polarization, namely higher binding energies for Co2p peaks and lower binding energies for S2p peaks compared to pure CoS_2 , due to the shortened Co–S bond. The peaks with a binding energy of 161.78 eV (pure CoS_2) and 161.65 eV (O– CoS_2) were assigned to S_2^{2-} that had not entered the CoS_2 lattice and bonded with Co^{2+} or CoS_2 surface.^[20] Besides, the increased S_2^{2-} peak area for O– CoS_2 reveals the effective adsorption of CO-precursor. The remaining two peaks at about 165.01 eV and 169.18 eV could be ascribed to the S–C bond derived from the decomposition of thiourea and oxidized sulfur species, respectively. Likewise, the composition of C element was discussed in C1s spectra and C–C/C=C peaks used for calibrating to 284.6 eV was main structure of carbon species.^[21] Furthermore, C–N and slight C–O bond was also clearly denoted in Figure 3d. All detailed peak position parameters were provided in Table S1.

On balance, except for the difference in binding energy, the same electronic structure of main elements indicated that O– CoS_2 and pure CoS_2 had the same nanoparticle formation process. Thermogravimetric (TG) analysis carried out in nitrogen from 35 to 800 °C was shown in Figure 3e. Compared with the TG curves of pure CoS_2 , a sharp decline in weight occurred between 530 and 630 °C, which was further evidence that the O– CoS_2 catalyst had more carbon species, according to the previous reports.^[22] Obtained from the final weight percentage at 800 °C, the treated hydroxide template increased 7.3%

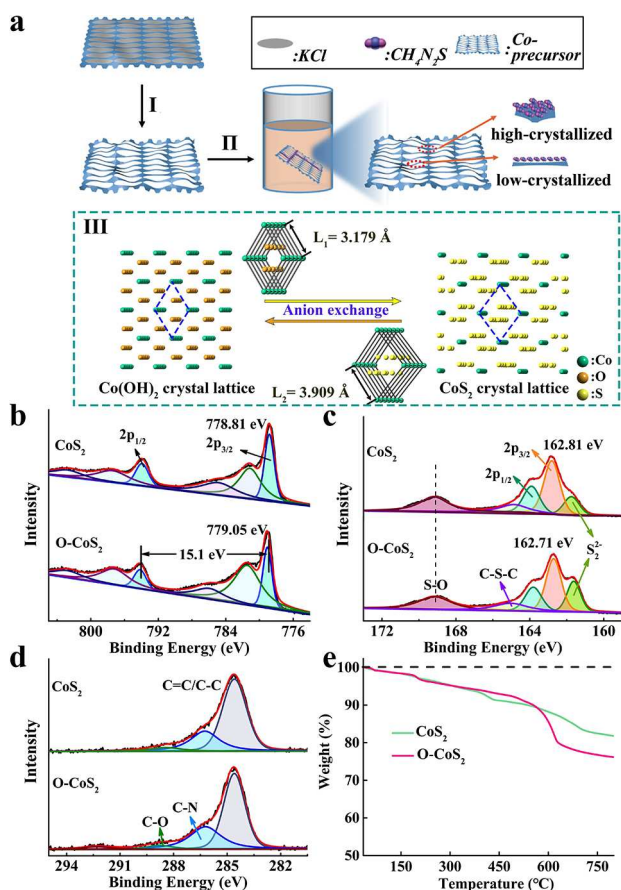


Figure 3. (a) Schematic diagram of the formation of O– CoS_2 . (b) Co 2p core-level XPS spectra of CoS_2 and O– CoS_2 . (c) XPS of S 2p spectra of CoS_2 and O– CoS_2 . (d) XPS of C 1s spectra of CoS_2 and O– CoS_2 . (e) Thermogravimetric (TG) curve of CoS_2 and O– CoS_2 .

carbon material (contained little nitrogen) for CoS₂ catalysts by prophase adsorption. Moreover, the reaction solution after hydrothermal synthesis was also provided in Figure S6. A yellowish solution was observed for pristine CoS₂ in comparison to the clear and colorless solution for O-CoS₂, owing to the dissolution of excessive S or N species.

Electrochemical performance

To gain insight into the electrochemical performance, as-prepared catalysts were assessed by a series of comparative measurements. The CV measurement (Figure 4a) was measured in N₂ and O₂ saturated 0.1 M KOH solution at a scan rate of 50 mV/s. The pristine CoS₂ and O-CoS₂ exhibited an evident oxygen reduction peak in O₂-saturated solution by contrast with its CV in the N₂-saturated solution, and O-CoS₂ had a better ORR activity due to higher cathodic peak current density. The ORR polarization plots can also observe the same conclusion through rotating-disk electrode (RDE) measurements in Figure 4b. The O-CoS₂ provided 40 mV more positive half-wave potential and higher limiting diffusion current density than pristine CoS₂. Even in comparison to Pt/C, O-CoS₂ showed a chose half-wave potential ($\Delta E=42$ mV) and better plateau

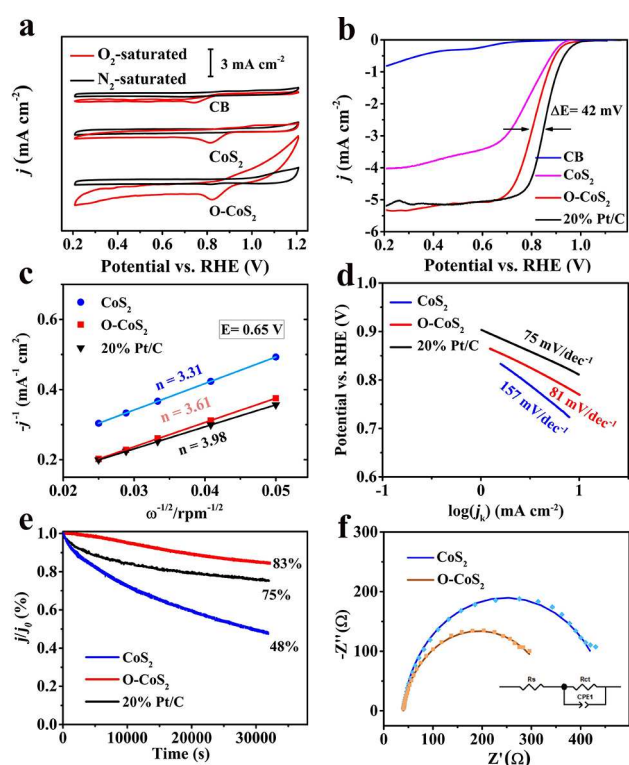


Figure 4. (a) CV curves of carbon black (CB), CoS₂ and O-CoS₂ in N₂- and O₂-saturated 0.1 M KOH solution. (b) LSV curves of as-prepared catalysts at 1600 rpm rotation rates in O₂-saturated 0.1 M KOH solution. (c) Electron transfer number of as-prepared catalysts at $E = 0.65$ V. (d) Tafel curves of as-prepared catalysts at 1600 rpm rotation rates in O₂-saturated 0.1 M KOH solution. (e) Stability measurements as-prepared catalysts in 0.1 M KOH solution at a rotating rate of 1000 rpm. (f) Electrochemical impedance curves of as-prepared catalyst.

current density, indicating crystal-cell shrinkage of CoS₂ provided a benefit to ORR performance. Detailed comparison results were shown in Table S2.

Furthermore, for analysis of electron-transfer kinetics on oxygen reduction process, a series of rotation rates (Figure S7) from 400 to 1600 rpm were measured in O₂-saturated 0.1 M KOH solutions, which can provide the current-rotation rate relationship, showed in Figure 4c, with the Koutecky-Levich (K-L) equation. Furthermore, all obtained K-L plots of as-prepared samples displayed good linear relation at 0.65 V, which was further calculated to get the electron transfer number (n). The number of O-CoS₂ is 3.61, which is close to that of commercial Pt/C catalyst (3.98), suggesting its outstanding ORR activity and the ORR for the O-CoS₂ catalyst undergoes a quasi-four-electron process. Besides, the kinetic current density (j_k) showed in Figure S8 revealed the O-CoS₂ had the highest kinetic current density among them. In addition, as a significant parameter for evaluating ORR intrinsic activity, the Tafel slope was presented in Figure 4d. The O-CoS₂ with a close Tafel slope of Pt/C at low overpotentials manifested efficient electron transport and intrinsic catalytic activity.^[23]

As showed in Figure 4e, stability measurements of as-prepared catalysts were carried out by chronoamperometry in 0.1 M KOH solution at a rotating rate of 1000 rpm. After the 32000 s operation, O-CoS₂ still retained 83% relative current while pristine CoS₂ was 48%, and Pt/C catalyst was 75%, indicating that the polyhedral structure of CoS₂ presented after shrinkage was more stable in the ORR process. Furthermore, methanol resistance measurements were shown in Figure S7 (b and d), Pt/C electrode suffered a higher fluctuation in the presence of methanol, and there were almost no effects on performance for O-CoS₂ catalyst.

Therefore, the O-CoS₂ catalyst exhibits better methanol tolerance than Pt/C. Electrochemical impedance spectroscopy (EIS) was an important indicator for estimating interfacial processes and kinetics of electrode reactions in electrochemical systems, which was performed at each catalyst's half-wave potential ranging from 1 Hz to 10 kHz, showed in Figure 4f. Fitting equivalent circuits (insert) with the ZView software yielded charge-transfer resistance (R_{ct}) values of pristine CoS₂ (412 Ω) > O-CoS₂ (305 Ω), indicating that O-CoS₂ possessed a faster electron transport during ORR. Otherwise, abundant carbon species on the surface of O-CoS₂ also enriched the free electron density, thereby enhancing conductivity. So, O-CoS₂ had a smaller arc diameter than pristine CoS₂.

Changes of crystal-filed configurations states for Co²⁺

More information about the crystal field effect, the spin state, and the oxidation state was determined by Co-K edge X-ray absorption near-edge structure (XANES). In Figure 5a, the O-CoS₂ showed higher oxidation states than pristine CoS₂, owing to a shortened Co-S bond. In addition, the decreased intensity of the "white line" region reflecting local symmetry and electronic state,^[24] was consistent with the shortened Co-Co bond lengths mentioned before. The crystal field

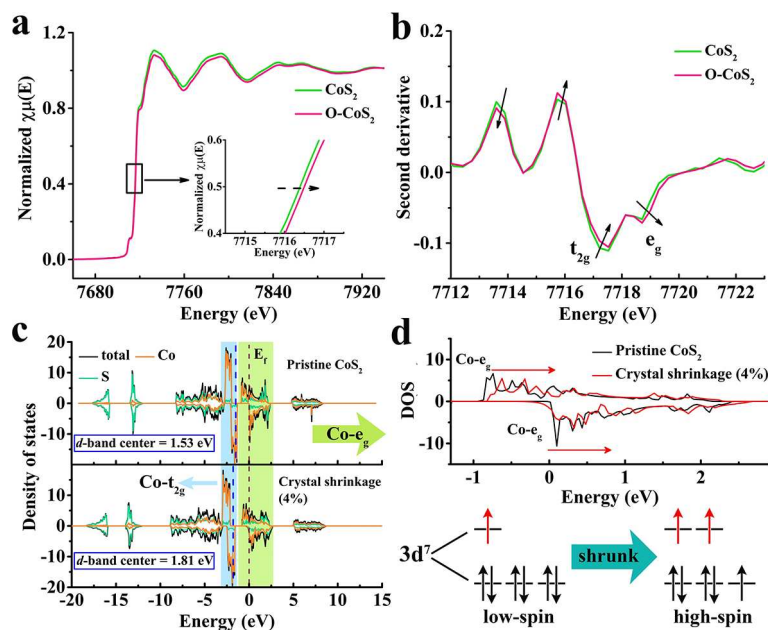


Figure 5. (a) Co-K edge XANES of CoS_2 and O-CoS_2 . (b) Second derivatives of CO-K edge XANES for CoS_2 and O-CoS_2 . (c) Density of states of CoS_2 and CoS_2 with a crystal shrinkage (4%). (d) Density of states of Co-e_g orbitals of CoS_2 and CoS_2 with a crystal shrinkage (4%), and the changes of configurations states of Co^{2+} .

configuration transitions for Co^{2+} were presented in the second derivatives of CO-K edge XANES spectra. The negative peak split into one prominent peak and one small peak, corresponding to fully filled t_{2g}^6 orbital and e_g^1 orbital occupied by a single electron, respectively.^[25] Reduced-intensity of t_{2g} peaks and enhanced intensity of e_g peaks demonstrated the increased e_g occupancy number of the 3d electron, which correlated to surface oxygen bond energy and ultimately affected the intrinsic activities of ORR. In the light of the previous reports,^[9a,26] the OER/ORR intrinsic activity can be inferred by the occupancy numbers of e_g orbital of transition metal ions, and the optimal occupancy was a near-unity. Therefore, crystal-cell shrinkage of CoS_2 would lead to an increase in occupancy of e_g orbital of Co ion.

To make a stronger case, the calculation about the density of states was shown in Figures 5c and d to investigate the occupancy of the orbital states. The density of states (DOS) of O-CoS_2 was simulated by applying stress on the original cell, and 4% shrinkage was based on the previous value of R (Figure 1c₁). Overall, the orbital states of Co3d and S3p after compression presented a stronger hybridization and overlap, in addition, had a consistent shift trend. The d -band center as a good descriptor for adsorption capacity of oxygen intermediates,^[27] the modest d -band center made for improving ORR kinetics. By calculation, compressed crystal cell emerged a lower d -band center, indicating a higher affinity for O_2 , which might account for the O-CoS_2 with higher onset potential. The e_g orbital of Co3d, showed in Figure 5d, consisted of the “alpha” orbital crossing the Fermi level and “beta” empty orbital. Apparently, the e_g orbital occupied states of contracted crystal cell moved to higher energy levels compared to pristine CoS_2 .

Hence, as illustrated by the schematic diagram of the electronic configuration of Co3d orbital (bottom part of Figure 5d), the spin state of Co^{2+} transformed from low spin to high spin brought about increased occupancy numbers of e_g orbital,^[28] which was consistent with the result of Co-K edge XANES and contributed to the formation of anti-bonding with oxygen molecular orbital in ORR process.

Conclusions

In a nutshell, we successfully synthesized O-CoS_2 catalysts with a well-defined polyhedron structure by using a polyporous soft template. Compared with the pristine CoS_2 , the O-CoS_2 presented a lattice shrinking phenomenon, which was mainly attributed to the use of soft-template. The soft template with abundant mesopore rendered a self-assembled arrangement of sulfur sources and contributed to anion exchange. In the process of anion exchange, the O-CoS_2 was generated by employing the Co-Co skeleton derived from cobalt hydroxide, and the smaller crystal-cell size of cobalt hydroxide also inhibited the expansion of CoS_2 crystal cell. So, this provided a smaller lattice parameters in comparison to the pristine cobalt disulfide without templates. What is more, O-CoS_2 consisted of large grains with high crystallinity and irregular granules with low crystallinity, which was caused by the difference microtopography of polyporous CO-precursor. The irregular granules possessed the same elementary composition and electronic structure as pristine CoS_2 . The large grains of O-CoS_2 presented a higher Co/S ratio and a shrinkage of crystal-cell phenomenon that was considered the main cause of improved ORR activity.

The high-angle offset of peak position in XRD, an overall hypsochromic shift in Raman spectra, decreased R value in extended X-ray absorption fine structure, and a reduced lattice spacing of the corresponding facets in TEM together proved the shrinkage of the crystal cell of O-CoS₂. The second derivatives of Co-K edge XANES spectra and the density of states of Co3d manifested the increased occupation numbers in e_g orbitals resulting in transformation of the Co3d orbitals from low spin to high spin, which was the intrinsic reason for enhanced ORR activity. Consequently, our works provided a new idea for improving the activity of this type of catalyst.

Experimental Section

Catalyst synthesis: All chemicals are of analytical grade and were used as received without further purification.

Synthesis of hydroxide soft template: In a typical experiment, 1.2 mmol CoCl₂·6H₂O and 2.4 mmol KOH were each dissolved in 3 mL methanol solution. After completely dissolution, the potassium hydroxide solution was slowly added to the cobalt solution and 0.3 mL deionized (DI) water was added into the above solution under vigorous stirring. The brown products were filtered and washed several times with deionized water until it turned black. The Co-precursor were dried in air at 70 °C overnight for further modification.

Synthesis of O-CoS₂: The as-prepared Co-precursor was dissolved in 25 mL DI water containing 2 mmol thiourea, and then the solution was transferred into a 50 mL Teflon-lined stainless-steel autoclave. The autoclave was sealed and hydrothermally treated at 200 °C for 12 h. After the reaction was finished, the O-CoS₂ was washed several times with ethanol and DI water and then dried at 70 °C for 10 h in a vacuum oven.

Synthesis of pristine CoS₂: The pristine CoS₂ was prepared by the same procedure without soft template. 1.2 mmol CoCl₂·6H₂O and 2 mmol thiourea were dissolved in 25 mL DI water. Then the solution pH value was adjusted to about 10 using KOH. The solution was transferred into a 50 mL Teflon-lined stainless-steel autoclave at 200 °C for 12 h.

Electrochemical characterization and electrode preparation: The CHI 650D electrochemical workstation was used to carry out electrochemical measurements. Platinum net and standard calomel electrode as the counter and reference electrodes, respectively, made up a standard three-electrode cell. A series of polarization curves (LSV) and CV measurements were performed in 0.1 mol L⁻¹ KOH electrolyte within the potential range of 0.2 and 1.2 V (vs. RHE). The oxygen continued to flow into the electrolyte for ensuring O₂ saturation, apart from the acquisition of background current that needs N₂ saturation. The final spectrum of LSV was obtained by subtracting the background current from the actual current.

The electron transfer number (n) per oxygen molecule under different voltage were calculated by K-L plots:

$$\frac{1}{i} = \frac{1}{i_k} + \frac{1}{i_d} = \frac{1}{nFAkC} + \frac{1}{0.2nFAD^{2/3}v^{-1/2}C_0^{1/2}} \quad (1)$$

Where i is the measured current density on RDE, i_k is kinetically limited current density and consists of the electron transfer number (n), the Faraday constant (F), the oxygen solubility (C) in the electrolyte, and the rate constant (k). i_d is the diffusion-limited

current density and consists of the electron transfer number, the Faraday constant, diffusivity of oxygen (D), kinematic viscosity (ν), the oxygen solubility, and the rotation rate (ω).

The working electrode comprised a thin-film layer of catalyst on a glassy carbon disk (5 mm in diameter). For preparing the thin-film layer, 5 mg of the sample (comprised catalyst/Vulcan carbon = 2:3 mass ratio) was ultrasonicated in 1.5 mL isopropanol/DI water (2:1 v/v) with 15 μ L 5% Nafion solution as solvent for 30 min, and then 8 mL dropping liquid was transferred to the glassy carbon disk and then dried in the air. The total mass loading for each electrode was 200 μ g cm⁻².

Characterization: The powder X-ray diffraction (XRD) patterns were obtained by D/max2550 V X-ray diffractometer using Cu_{K α} radiation. The Raman spectra were measured by Laser Micro-Raman Spectrometer using 532 nm laser. The X-ray absorption (XAS) data of the samples were recorded at room temperature in the transmission mode using ion chambers and the BL14 W1 beam line in the Shanghai Synchrotron Radiation Facility (SSRF), China. The Brunner-Emmet-Teller (BET) surface area was carried out by Micromeritics Tristar 3020 SIN 993. The mapping images and physical morphology were determined by field-emission scanning electron microscopy (FESEM GeminiSEM 500) and high-resolution transmission electron microscopy (HRTEM, JEM-2100). The chemical composition and valence states of elements were examined by X-ray photoelectron spectroscopy (XPS, ESCALAB 250Xi) using a monochromatic Al_{K α} X-ray source. Binding energies were normalized with regard to exogenous C 1 s.

Density functional theory (DFT) calculation: All crystal structure information and phase parameters were produced by the National Institute of Standards and Technology (NIST). The crystal-cell model for density of states of O-CoS₂ was obtained by shrinking the original crystal cell by 4%, which was according to the value of R in k^2 -normalized Co-K edge EXAFS. The self-consistent field was considered to converge when energetic convergence threshold changed within 1×10^{-4} eV per atom. First-principles calculations were implemented in the Vienna Ab-initio Simulation Package (VASP). The spin-polarized DFT computations were performed with Perdew-Burke-Ernzerhof (PBE) generalized gradient approximation (GGA) for exchange-correlation interactions. A plane-wave cut-off energy of all computations was set to 400 eV.

Acknowledgements

This research is based on the work supported by the National Natural Science Foundation of China (51778229). We thank beamline BL14W1 (Shanghai Synchrotron Radiation Facility) for providing the beam time.

Conflict of Interest

The authors declare no conflict of interest.

Keywords: cobalt disulfide · crystal cell · electrocatalysis · oxygen reduction reaction · self-assembly

[1] Y. Liu, Y. Li, H. Kang, T. Jin, L. Jiao, *Mater. Horiz.* **2016**, *3*, 402–421.

[2] a) Z. Hu, X. Zhou, Y. Lu, R. Jv, Y. Liu, N. Li, S. Chen, *Electrochim. Acta* **2019**, *296*, 214–223; b) Y. Shiga, N. Umezawa, N. Srinivasan, S. Koyasu, E.

- Sakai, M. Miyauchi, *Chem. Commun.* **2016**, 52, 7470–7473; c) W. Li, Y. Li, H. Wang, Y. Cao, H. Yu, F. Peng, *Electrochim. Acta* **2018**, 265, 32–40.
- [3] a) S. Chandrasekaran, L. Yao, L. Deng, C. Bowen, Y. Zhang, S. Chen, Z. Lin, F. Peng, P. Zhang, *Chem. Soc. Rev.* **2019**, 48, 4178–4280; b) S. Shen, Q. Wang, *Chem. Mater.* **2013**, 25, 1166–1178.
- [4] X. Cao, X. Zheng, J. Tian, C. Jin, K. Ke, R. Yang, *Electrochim. Acta* **2016**, 191, 776–783.
- [5] D. C. Higgins, F. M. Hassan, M. H. Seo, J. Y. Choi, M. A. Hoque, D. U. Lee, Z. Chen, *J. Mater. Chem. A* **2015**, 3, 6340–6350.
- [6] V. Singh, A. Tiwari, T. C. Nagaiah, *J. Mater. Chem. A* **2018**, 6, 22545–22554.
- [7] W. Sun, Y. Song, X. Gong, L. Cao, J. Yang, *Chem. Sci.* **2015**, 6, 4993–4999.
- [8] L. An, Y. Li, M. Luo, J. Yin, Y. Zhao, C. Xu, F. Cheng, Y. Yang, P. Xi, S. Guo, *Adv. Funct. Mater.* **2017**, 27, 1703779.
- [9] a) J. Suntivich, H. A. Gasteiger, N. Yabuuchi, H. Nakanishi, J. B. Goodenough, Y. ShaO–Horn, *Nat. Chem.* **2011**, 3, 546–550; b) J. Suntivich, K. J. May, H. A. Gasteiger, J. B. Goodenough, Y. ShaO–Horn, *Science* **2011**, 334, 1383.
- [10] C. Chen, P. Chen, M. Basu, K. Yang, Y. Lu, C. Dong, C. Ma, C. Shen, S. Hu, R. Liu, *J. Mater. Chem. A* **2015**, 3, 23466–23476.
- [11] S. G. Lyapin, A. N. Utyuzh, A. E. Petrova, A. P. Novikov, T. A. Lograsso, S. M. Stishov, *J. Phys. Condens. Matter* **2014**, 26, 396001.
- [12] C. Ouyang, X. Wang, S. Wang, *Chem. Commun.* **2015**, 51, 14160–14163.
- [13] C. Zhao, D. Li, Y. Feng, *J. Mater. Chem. A* **2013**, 1, 5741–5746.
- [14] J. Li, Z. Xia, M. Zhang, S. Zhang, J. Li, Y. Ma, Y. Qu, *J. Mater. Chem. A* **2019**, 7, 17775–17781.
- [15] T. Y. Ma, Y. Zheng, S. Dai, M. Jaroniec, S. Z. Qiao, *J. Mater. Chem. A* **2014**, 2, 8676–8682.
- [16] S. Wan, Y. Liu, G. Li, X. Li, D. Wang, X. Zou, *Catal. Sci. Technol.* **2016**, 6, 4545–4553.
- [17] Y. Cui, C. Zhou, X. Li, Y. Gao, J. Zhang, *Electrochim. Acta* **2017**, 228, 428–435.
- [18] H. Wang, Y. Liang, Y. Li, H. Dai, *Angew. Chem. Int. Ed.* **2011**, 50, 10969–10972; *Angew. Chem.* **2011**, 123, 11161–11164.
- [19] B. Chen, Z. Jiang, L. Zhou, B. Deng, Z. Jiang, J. Huang, M. Liu, *J. Power Sources* **2018**, 389, 178–187.
- [20] a) J. Wang, J. Wang, L. Han, C. Liao, W. Cai, Y. Kan, Y. Hu, *Nanoscale* **2019**, 11, 20996–21007; b) F. Xu, B. Jin, H. Li, W. Ju, Z. Wen, Q. Jiang, *New J. Chem.* **2019**, 43, 18294–18303.
- [21] Y. Niu, X. Qian, J. Zhang, W. Wu, H. Liu, C. Xu, L. Hou, *J. Mater. Chem. A* **2018**, 6, 12056–12065.
- [22] X. Yao, H. Cheng, Z. Jiang, Q. Han, Y. Wang, S. Wang, *New J. Chem.* **2020**, 44, 10404–10409.
- [23] D. He, Y. Xiong, J. Yang, X. Chen, Z. Deng, M. Pan, Y. Li, S. Mu, *J. Mater. Chem. A* **2017**, 5, 1930–1934.
- [24] W. Q. Zaman, W. Sun, M. Tariq, Z. Zhou, U. Farooq, Z. Abbas, L. Cao, J. Yang, *Appl. Catal. B* **2019**, 244, 295–302.
- [25] a) J. Choy, D. Kim, G. Demazeau, D. Jung, *J. Phys. Chem.* **1994**, 98, 6258–6262; b) S. P. Farrell, M. E. Fleet, *Phys. Chem. Miner.* **2001**, 28, 17–27; c) S. Chattopadhyay, C. Mande, *Phys. Status Solidi B* **1984**, 126, 53–57.
- [26] W. Yuan, Y. Wang, P. Chernev, K. Klingan, M. Reza Mohammadi, S. Loos, C. Pasquini, P. Kubella, S. Jiang, Z. Cui, S. Zhu, Z. Li, S. Wu, H. Dau, J. Zhang, Y. Liang, *J. Catal.* **2020**, 383, 221–229.
- [27] C. Si, Y. Zhang, C. Zhang, H. Gao, W. Ma, L. Lv, Z. Zhang, *Electrochim. Acta* **2017**, 245, 829–838.
- [28] X. Gao, J. Liu, Y. Sun, X. Wang, Z. Geng, F. Shi, X. Wang, W. Zhang, S. Feng, Y. Wang, K. Huang, *Inorg. Chem. Front.* **2019**, 6, 3295–3301.

Manuscript received: December 29, 2020
Accepted manuscript online: January 6, 2021
Version of record online: February 2, 2021